

System Parameters of the Transiting Extrasolar Planet HD 209458b

Robert A. Wittenmyer¹, William F. Welsh, Jerome A. Orosz

Department of Astronomy, San Diego State University, San Diego, CA 92182

robw@astro.as.utexas.edu, wfw@sciences.sdsu.edu, orosz@sciences.sdsu.edu

A. B. Schultz, W. Kinzel, M. Kochte

*Science Programs, Computer Sciences Corporation, and Space Telescope Science Institute,
3700 San Martin Drive, Baltimore, MD 21218*

F. Bruhweiler

*IACS/Department of Physics, Catholic University of America, and NASA Goddard
Spaceflight Center, Greenbelt, MD 20771*

D. Bennum

Physics Department, University of Nevada-Reno, Reno, NV 89557

Gregory W. Henry

*Center of Excellence in Information Systems, Tennessee State University, 330 10th Avenue
North, Nashville, TN 37203; also Senior Research Associate, Department of Physics and
Astronomy, Vanderbilt University, Nashville, TN 37235*

G. W. Marcy, D. A. Fischer

*Astronomy Department, University of California at Berkeley, 601 Campbell Hall, Berkeley,
CA 94720-3411*

R. P. Butler

*Department of Terrestrial Magnetism, Carnegie Institution of Washington, 5241 Broad
Branch Road NW, Washington, DC 20015-1305*

and

S. S. Vogt

¹Department of Astronomy, University of Texas at Austin, 1 University Station, C1400, Austin, TX 78712

University of California/Lick Observatory, University of California at Santa Cruz, Santa Cruz, CA 95064

ABSTRACT

We derive improved system parameters for the HD 209458 system using a model that simultaneously fits both photometric transit and radial velocity observations. The photometry consists of previous *Hubble Space Telescope* STIS and FGS observations, twelve I -band transits observed between 2001–2003 with the Mt. Laguna Observatory 1m telescope, and six Strömgren $b + y$ transits observed between 2001–2004 with two of the Automatic Photometric Telescopes at Fairborn Observatory. The radial velocities were derived from Keck/HIRES observations. The model properly treats the orbital dynamics of the system, and thus yields robust and physically self-consistent solutions. Our set of system parameters agrees with previously published results though with improved accuracy and precision. For example, applying robust limits on the stellar mass of 0.93–1.20 M_{\odot} , we find $1.26 < R_{\text{planet}} < 1.42 R_{\text{Jup}}$ and $0.59 < M_{\text{planet}} < 0.70 M_{\text{Jup}}$. We can substantially reduce the uncertainty on these estimates by including a stellar mass–radius relation constraint, yielding $R_{\text{planet}}=1.35\pm0.06 R_{\text{Jup}}$ and $M_{\text{planet}}=0.66\pm0.03 M_{\text{Jup}}$. Our results verify that the planetary radius is 20% larger than predicted by planet evolution models, confirming the need for irradiation and/or some other mechanism to slow the evolutionary contraction of the planet. A revised ephemeris is derived, $T_0 = 2452854.82545 + 3.52474554E$ (HJD), which now contains an uncertainty in the period of 0.016 s and should facilitate future searches for planetary satellites and other bodies in the HD 209458 system.

Subject headings: stars: individual, HD 209458—extrasolar planets

1. Introduction

Of more than 150 recently discovered extrasolar planets¹, HD 209458b is the first known to transit its star (Henry et al. 2000; Charbonneau et al. 2000). Combined with the spec-

¹A current tally can be found at the California and Carnegie Planet Search homepage, <http://exoplanets.org>, or at the J. Schneider Extrasolar Planet Encyclopaedia, <http://www.obspm.fr/encycl/encycl.html>.

troscopic radial-velocity curve, photometric observations of transits allow high-precision determination of system parameters such as the inclination, planetary radius and mass. For example, using *Hubble Space Telescope* photometry of HD 209458b, Brown et al. (2001) derived estimates of the inclination $i = 86^\circ.6 \pm 0^\circ.14$ and planetary radius $R_{\text{planet}} = 1.347 \pm 0.060 R_{\text{Jup}}$; with the additional estimate that the host star's mass is $M_{\text{star}} = 1.06 \pm 0.13 M_{\odot}$, Cody & Sasselov (2002) find $M_{\text{planet}} = 0.69 \pm 0.02 M_{\text{Jup}}$.

With a measured radius and mass, HD 209458b observations are extremely important in refining the theory of irradiated extrasolar giant planets (EGPs). Most notably, the observed radius of HD 209458b is $\sim 20\%$ larger than models predict (Guillot & Showman 2002; Bodenheimer, Lin, & Mardling 2001; Bodenheimer, Laughlin, & Lin 2003; Baraffe et al. 2003; Laughlin et al. 2005). Guillot & Showman (2002) use evolutionary models of irradiated EGPs to argue for an additional heat source acting on HD 209458b. They found that the radius of HD 209458b can be produced with the transport of $\sim 1\%$ of incident stellar flux into the lower atmosphere as kinetic energy (i.e. winds). As HD 209458b is probably tidally locked, one side is perpetually illuminated, and high-speed winds would be expected to transfer heat from the day side to the night side (Showman & Guillot 2002; Cho et al. 2003; Menou et al. 2003). Bodenheimer, Lin, & Mardling (2001) suggest that continuing tidal circularization of HD 209458b is heating the planet, inflating it to a radius larger than predicted for a circular orbit. Recent observations of the transiting exoplanet TrES-1 (Alonso et al. 2004; Sozzetti et al. 2004; Laughlin et al. 2005), indicating that its radius is consistent with models that do not invoke additional heat sources, support Burrows et al. (2004) suggestion that the large radius of HD 209458b may be anomalous. The radii estimates of the OGLE-discovered exoplanets are also consistent with models that include only irradiation. Determining the planetary radius of HD 209458b more accurately would assist in resolving this discrepancy.

An extremely precise ephemeris can allow the inference of additional bodies in the system by their gravitational effects on the transit times and slight asymmetries in the transit light curve (Sartoretti & Schneider 1999; Agol et al. 2004; Holman & Murray 2004). The transit of HD 209458b affords the opportunity to make highly accurate and precise measurements of the planet's orbital period. The ability to predict and observe HD 209458b transits at 1-second precision would place strong constraints on the masses of satellites or additional planets in the system. Brown et al. (2001) point out that an Earth-mass satellite of HD 209458b would alter the time of mid-transit by up to 13 seconds, and a $1 M_{\text{Jup}}$ planet at 10 AU would alter the transit time by up to 5 seconds due to its gravitational influence on the star. An ephemeris precise at the 1-second level would facilitate tests for such timing displacements. The precision of the STIS transit timings obtained by Brown et al. (2001) allowed the exclusion of satellites larger than 3 Earth masses at the 3σ level by

analysis of the timing displacements of the four transits they observed. Even if no moons are present around HD 209458b, the technique of transit timing can be readily applied to future transiting systems. Some extrasolar giant planets reside in the habitable zones of their parent stars, a region where the star’s insolation is such that liquid water could exist on the surface of a planet. Terrestrial-size moons of giant planets in such an orbit could in theory be habitable (Williams, Kasting, & Wade 1997). The only currently available methods of detecting such objects require transits; refining modelling techniques using HD 209458b thus builds a solid foundation for characterization of future discoveries of transiting extrasolar planets, e.g. the *Kepler* mission. The most widely used ephemeris by Robichon & Arenou (2000), based on *Hipparcos* photometric data and the radial-velocity curve (Mazeh et al. 2000), contained uncertainties in the period of ± 1.21 seconds. Propagating to the present epoch yields an uncertainty in the time of mid-transit of over ± 16 minutes. There exists, therefore, a need to revise the ephemeris, as the predicted time of mid-transit continuously accumulates errors in period. Even with a period determination accurate to 1 second, the large number of cycles (~ 100 per year) results in nearly 2 minutes of uncertainty accumulating after only a year.

In this work, we fit a single, self-consistent model to observations of twenty-seven HD 209458b transit events in four bandpasses, and to more than three years of high-precision radial velocities. In §2 we briefly describe the five data sets used in this study, §3 outlines the modelling procedure, and in §4 we present and discuss the system parameters.

2. Observations

2.1. Mount Laguna Observatory (MLO)

Twelve *I*-band transits of HD 209458b were observed with the 1-meter telescope at Mount Laguna Observatory (MLO). A log of these and all other photometric data is presented in Table 1. Observing runs in 2002 and 2003 consisted of a 4 to 6 hour series of 1-second exposures on a Loral 2048x2048 CCD. A field of view of 5x6.5 arcmin was used, which included three faint comparison stars. Observations in 2001 used 4-second exposures and a field of view of 5.9x5.9 arcmin that only included TYC 1688-1903-1 as a comparison star, and so this star was used as the comparison on all nights.

The brightness of HD 209458 ($V=7.645$) required defocusing the telescope slightly to avoid saturating the CCD; as such, large photometry apertures ($\sim 3 \times FWHM$ or 9 arcsec) were employed. Light curves were obtained using standard differential photometry with one comparison star. The photometry was then binned to a time resolution of about 167 s to help reduce the scintillation noise of the short exposures, yielding a total of 1149 points. The

error bars on the binned points were calculated in the following way: uncertainties based on propagation of the IRAF-generated error estimates were used to compute the inverse-variance weighted mean per bin. Then this error bar was boosted by $\sqrt{(\chi^2_\nu)}$ if the reduced χ^2_ν of the scatter of the points about the mean in the bin was greater than 1.

For most transits, slight tilts ($\sim 0.5\%$) in the light curves were evident, likely due to systematic calibration errors. Comparison star variability was ruled out, as the tilts did not occur in all nights. Color-dependent differential extinction was also excluded, as the correlation between the tilts and the airmass was not consistent. These tilts were corrected by masking the transit and fitting a line to the out-of-transit light curve. This linear fit was then subtracted from the data, rectifying the light curves. Finally, under the assumption that the out-of-transit light curve is constant, the root mean square (RMS) deviation of the out-of-transit observations was compared with the mean uncertainty of these data. We found the error bars to be slightly underestimated, almost certainly due to systematic errors unaccounted for in the data reduction. We boosted all the uncertainties by 11% to make the uncertainties consistent with the out-of-transit RMS deviation.

2.2. *Hubble Space Telescope* STIS

Brown et al. (2001) obtained and analyzed extremely high-precision observations of four HD 209458b transits using the *Hubble Space Telescope* Space Telescope Imaging Spectrograph (STIS). A total of 20 *Hubble Space Telescope* orbits in four visits spanning 18 days yielded a total of 684 spectra, covering a wavelength range of ~ 582 –638 nm. Binned over wavelength, the spectra yield photometry with a relative precision of about 1.1×10^{-4} per 60 s integration. Following Brown et al. (2001) we omitted the first orbit of each of the four HST visits in our modelling because of a systematic 0.25% deficit in flux, leaving 556 points in the light curve. As with the MLO observations, the RMS deviation of the out-of-transit light curve about a constant was used to check for the accuracy of the error estimates. We boosted the uncertainties by 4.5% to make the error estimates agree with the RMS deviation out of transit.

2.3. *Hubble Space Telescope* FGS

Five transits were observed by Schultz et al. (2003) using photomultiplier tubes (PMTs) in the *Hubble Space Telescope* Fine Guidance Sensor (FGS). The FGS, normally used for astrometry and pointing control, was for the first time used as a high-speed photometer on

a bright star. The four PMTs in FGS1r were used with a sampling rate of 40 Hz, and a $S/N \sim 80$ per 0.025 s exposure was achieved. The F550W filter was used, giving a central wavelength of approximately 550 nm. A time dependency in the FGS response was corrected by fitting a 5th order Chebyshev polynomial to the out-of-transit data for each transit and each PMT. The data were then placed into 80 s bins for consistency with the STIS data of Brown et al. (2001). Schultz et al. (2004) have used these FGS data and the STIS data of Brown et al. (2001) to obtain a precise set of system parameters: $R_{\text{planet}} = 1.367 \pm 0.043 R_{\text{Jup}}$, $R_{\text{star}} = 1.154 \pm 0.036 R_{\odot}$, and inclination $i = 86.525 \pm 0.054$, assuming a stellar mass of $M_{\text{star}} = 1.1 \pm 0.1 M_{\odot}$ from Mazeh et al. (2000). An orbital ephemeris of $T_0 = 2452223.895819 \pm 0.000031$ HJD and $P = 3.52474408 \pm 0.00000029$ days was also obtained; the uncertainty in the period is only 0.025 s. The precision of these data allowed the exclusion of transiting satellites of HD 209458b down to 2 Earth radii. Such an object would cause a $\sim 0.1\%$ dip in the transit light curve, which was not seen in the FGS data. We trimmed a total of 19 data points from the FGS observations, as these points were $> 4\sigma$ outliers from an initial model fit to the FGS data set. These points occurred at the beginning and end of each orbit, where the reliability of the FGS data is the poorest, probably due to HST “breathing.” A total of 268 FGS points were used in the modelling. The uncertainty estimates of the original Schultz et al. (2004) data were boosted by 38% to account for systematic errors and be consistent with the out-of-transit RMS deviation about a constant flux.

2.4. Automatic Photometric Telescope (APT)

Six transits were obtained in 2001–2004 with the T8 and T10 Automatic Photometric Telescopes (APTs) located at Fairborn Observatory in the Patagonia Mountains of southern Arizona (Henry 1999; Eaton, Henry, & Fekel 2003). The transits of HD 209458b were co-discovered in 2000 using data from the T8 APT (Henry et al. 2000). Precision photometers use dichroic mirrors to split the incoming light into two beams and two EMI 9124QB bi-alkali photomultiplier tubes to measure Strömgren b and y simultaneously. Differential magnitudes from the two passbands were combined into a single $(b + y)/2$ band for greater precision, which is typically 0.0012 mag for a single measurement. The comparison star was HD 210074 ($V = 5.74$ mag, F2V). These APT data had a time resolution of 95 s and provide a total of 1426 observations. The uncertainties were boosted by 7% so as to be consistent with the out-of-transit RMS deviation about a constant.

2.5. Keck/HIRES Radial Velocities

A set of 51 published (Henry et al. 2000) and unpublished Keck/HIRES radial velocity measurements was included in the model fits and is listed in the Appendix. These data were obtained with the HIRES echelle spectrometer at a resolution of $R \sim 80000$. An iodine absorption cell was used for wavelength calibration (Marcy & Butler 1992; Valenti, Butler, & Marcy 1995; Butler et al. 1996). The current data set includes 42 measurements not included in Henry et al. (2000), and covers a time span of 3.4 years. The mean uncertainty of these velocity measurements is 4.7 m s^{-1} .

3. Modelling of Transit Photometry and Spectroscopy

3.1. Outline of the Physical Model

The Eclipsing Light Curve (ELC) code (Orosz & Hauschildt 2000) was used to model HD 209458 by simultaneously fitting all transit light curves and the radial velocities. ELC explicitly includes the orbital and rotational dynamics of the system, yielding robust and physically self-consistent solutions. In ELC, the surfaces of the star and planet are defined by equipotential surfaces in the rotating binary frame. By using Roche equipotential surfaces to determine the radii, ELC can account for any non-sphericity of the bodies. In practice, for HD 209458 the difference between the polar and equatorial radii is only $\sim 0.007\%$, and can be neglected. ELC includes the effect of gravity darkening, though again because of the near sphericity of the star, this effect results in a negligible ($\sim 0.002\%$) change in temperature between stellar pole and equator.

In the original version of ELC, two parameters called the “filling factors” (f_{star} and f_{planet}) were used to define the equipotential surfaces. The filling factors are defined as the ratios of radii to Roche lobe radii, such that $f < 1$ for detached systems and $f = 1$ for a Roche lobe-filling body. For given masses, the filling factors thus define the stellar and planetary radii. Unfortunately, this way of specifying the equipotential surfaces is far from optimal in the case of HD 209458. Since the two bodies are nearly perfect spheres, a change in the mass ratio $Q = M_{\text{star}}/M_{\text{planet}}$ requires a change in f_{star} and f_{planet} to get the same transit profile. Thus it proved to be much more computationally efficient to have as the two parameters the *fractional radius* of the star R_{star}/a and the *ratio of the radii* $R_{\text{star}}/R_{\text{planet}}$ since the transit light curve is independent of the mass ratio when the equipotential surfaces are defined this way.

Once the surfaces of the star and planet are defined they are then divided into a grid of

surface elements (“tiles”). For HD 209458 a very fine grid of surface elements was required: even with $400 \text{ latitude} \times 600 \text{ longitude}$ tiles on the star we found numerical noise in the light curves of the order of 1 part in 10^5 , which is not good enough to model the precision of the *Hubble Space Telescope* light curves. To mitigate this effect, we employed a Monte Carlo subsampling of the partially eclipsed tiles, using 1000 random subsamples per tile. This technique allowed a much smaller number of grid elements and we adopted a final 250×240 grid on the star and 80×80 grid on the planet.

The intensity at each tile is approximated as a blackbody, accounting for limb darkening and correcting the effective temperature T_{eff} for gravity darkening (von Zeipel 1924; Claret 2000). Limb darkening was treated using the 2-parameter logarithmic prescription of van Hamme (1993):

$$I(\mu) = I_0(1 - x + x\mu - y\mu\ln\mu) \quad (1)$$

where μ is the foreshortening angle of the grid element and x and y are the two limb-darkening coefficients for each bandpass. Blackbody intensities were employed for convenience, but also because the Kurucz model atmosphere tables are presently too coarse at the $T_{\text{eff}}=6000 \text{ K}$ temperature appropriate for HD 209458 (Mazeh et al. (2000), Cody & Sasselov (2002)). After correcting the intensity of each tile for limb and gravity darkening, the binary is then “turned in space” by a user-specified phase step. A phase step size of $0^\circ.05$ was chosen, corresponding to about 42.3 s, to match the high time resolution (80 s) and precision ($\sim 1.1 \times 10^{-4}$) of the *Hubble Space Telescope* data. If a tile is completely eclipsed by the planet, it is not included in the calculation of total flux from the star. Partially eclipsed tiles are accounted for via the Monte Carlo method mentioned above. In this way, a model light curve is generated for the input parameters.

In the original version of ELC, the scale of the binary was fully specified by using the inclination i , the orbital separation a , and the mass ratio Q . In the case of HD 209458, we found it more convenient to use the mass of the star M_{star} and the projected semiamplitude of the star’s radial velocity curve K_{star} . For a given inclination i , the separation a and the mass ratio can be determined from M_{star} and K_{star} . Then given the orbital period P , the radial velocity of the star at each orbital phase is computed by summing the velocities of each stellar tile not eclipsed by the planet, again weighting for limb darkening and foreshortening (Wilson & Sofia 1976). In this way we fit the radial velocity observations, and do not just constrain the stellar motion to equal some adopted projected orbital velocity K_{star} .

Since ELC computes the projected radial velocities at each orbital phase, the Rossiter effect can be fit with our model. The Rossiter effect is a radial-velocity distortion which occurs as a result of the planet blocking the approaching and receding limbs of the star during transit (Rossiter 1924). The Rossiter effect was first observed in HD 209458 by Bundy &

Marcy (2000) and Queloz et al. (2000), and was used to deduce that the planet orbits in the same direction as the star’s rotation. The amplitude of the Rossiter effect is directly proportional to the star’s rotational velocity $V_{\text{rot}} \sin i$ and the size of the eclipsing object. As portions of the rotating stellar surface are blocked by the planet, the absorption line profiles are skewed in shape. Thus, the velocities reported here during the transit represent an apparent Doppler shift caused by the *skewing* of the original absorption lines, rather than a change in velocity. Because of this, we caution that the radial velocities through the transit as computed by ELC may not be identical to the radial velocities as measured in the stellar spectra via the cross-correlation method. A thorough investigation would require the convolution of a high signal-to-noise out-of-transit spectrum (or model spectrum) with a set of phase-dependent line-broadening functions generated during the transit. These synthetic spectra should then be cross-correlated with a template spectrum and the resulting simulated radial velocities compared with the ELC radial velocities. Such an investigation is beyond the scope of this paper, but we note that the Rossiter effect observations are in fact very well matched by the ELC model as seen in §4.2.

A circular ($e = 0$) planetary orbit was assumed, consistent with a tidal circularization time of order 10^8 yr for HD 209458b (Bodenheimer, Laughlin, & Lin 2003) and radial velocity observations (Mazeh et al. 2000). Recent *Spitzer Space Telescope* observations by Deming et al. (2005) shows the secondary eclipse occurs at orbital phase 0.5000 ± 0.0015 , demanding a very low eccentricity. The planet is also assumed to be tidally locked (rotation synchronous with its orbit) so the rotational frequency parameter Ω_{planet} , defined as the ratio of rotational frequency to the orbital frequency, was set to unity. The effective temperature of the planet was set to 1300 K, based on theoretical estimates of the night-side temperature of irradiated extrasolar giant planets (Guillot & Showman (2002); Deming et al. (2005) measure a brightness temperature of 1130 ± 150 K). At this temperature the flux ratio of the planet and star is approximately 3×10^{-11} in the V band and so the planet is essentially invisible in our optical photometry.

Finally, note that ELC computes the actual orbital path of the planet about the barycenter rather than simply a chord across the stellar disk. This includes the reflex motion of the star during transit, which for a 3.07 hr transit, amounts to a distance equal to 0.9% the radius of the planet. Though these effects are subtle, if improperly treated they can be sources of systematic error and can bias the system parameters. By including the dynamics of the orbits, ELC should in principle yield more accurate, as well as precise, system parameters.

3.2. Observational Constraints

HD 209458 is a single-lined binary system, and it is well-known that the radial velocity curve of the star sets the minimum mass of the planet:

$$f(M_{\text{planet}}) \equiv \frac{PK_{\text{star}}^3}{2\pi G} = \frac{M_{\text{star}}^3 \sin^3 i}{(M_{\text{planet}} + M_{\text{star}})^2}.$$

Once the mass function $f(M_{\text{planet}})$ is known, one needs the inclination and the mass of the star (or the ratio of masses) in order to find the mass of the planet M_{planet} . Once the component masses are known, the orbital separation a can be found from Kepler's third law. Since the transit light curves constrain the ratio of the radii ($R_{\text{star}}/R_{\text{planet}}$) and the fractional radii (R_{star}/a and R_{planet}/a), the radii of the star and planet in physical units are found once a is known.

From a strictly observational point of view, the inclination, relative radii, and limb darkening are constrained quite well from the multi-color transit light curves. However, neither the stellar mass or the mass ratio is constrained by the transit or radial velocity observations and so the scale of the system is indeterminate (see also the discussion in Deeg, Garrido & Claret (2001)). Since we are interested in the physical size and mass of the planet, an additional constraint is required to break the degeneracy. Fortunately we do have constraints on the radius and mass of the host star, by matching stellar evolution models with the star's luminosity and temperature.

Cody & Sasselov (2002) derive a stellar radius of 1.18 ± 0.10 R_{\odot} using the apparent V magnitude, the *Hipparcos* parallax (Perryman et al. 1997), and a well-determined bolometric correction. The $\sim 8\%$ error on this stellar radius estimate yields an 8% error on the orbital separation and hence will yield an uncertainty of $\pm 8\%$ in the planetary radius. We include this stellar radius estimate as an observation to be matched by the ELC model. The model is directed toward this value by use of a straightforward χ^2 penalty for deviations from the estimate. In a similar fashion, we include the observation of the projected stellar rotation velocity $V_{\text{rot}} \sin i$ of Queloz et al. (2000) as a datum to be matched. Thus in addition to the transit photometry and radial velocities, we include two more observables, with the radius of HD 209458 “steered” toward 1.18 ± 0.10 R_{\odot} , and toward a $V_{\text{rot}} \sin i$ of 3.75 ± 1.25 km s^{-1} . However, we emphasize that these are not constraints — the model is permitted to adopt values outside of these ranges, but at a cost in χ^2 .

Cody & Sasselov (2002) also determined a robust limit on the stellar mass of 1.06 ± 0.13 M_{\odot} ; this uncertainty range includes the observational errors in temperature, luminosity, and metallicity as well as systematic errors in convection mixing-length and helium abundance. The $\pm 12\%$ uncertainty on the stellar mass translates to roughly a $\pm 4\%$ error on the planet

radius. However, this range of allowable stellar mass is not quite a 1σ uncertainty, but more of a limit on the range of possible mass. For this reason, and also because the stellar mass determination is more model-dependent than the other parameters, we do not include the stellar mass as an observed parameter.

The relative uncertainty in the orbital velocity K_{star} also maps into an uncertainty in orbital separation and hence radii. The correspondence is 1:1, so an uncertainty of 1.6% in K_{star} gives a *minimum* uncertainty of 1.6% in radii. This 1.6% is the uncertainty in the radii *if* the mass of the star was exactly known.

3.3. Fitting Procedure

Using the above assumptions and conditions, all four photometric time series were modelled simultaneously with the radial velocities in order to obtain system parameters for HD 209458. The criteria defining the goodness of fit was the usual χ^2 . The ELC model contains 15 free parameters: the orbital period of the planet P , the time of mid-transit T_0 , the fractional radius of the star R_{star}/a , the ratio of the radii $R_{\text{star}}/R_{\text{planet}}$, the inclination, the semiamplitude of the star’s radial velocity curve K_{star} , the ratio of rotational frequency of the star to orbital frequency, and eight wavelength-dependent limb-darkening coefficients (two per bandpass). Because of the degeneracies in the solutions, the stellar mass was not a free parameter in the models. Rather, we fix the stellar mass and optimize all other parameters, then repeat with a different stellar mass. In this way we step through a range of stellar masses. The list of other fixed input parameters and their values is given in Table 2.

The weighting of the five data sets was determined by their uncertainties; no adjustments to the relative weights were made. In order to assure complete exploration of parameter space, a genetic algorithm based on the *pikaia* routine given in Charbonneau (1995) was used to find the global χ^2 minimum (see Orosz et al. (2002) for details), and a downhill simplex “amoeba” (Press et al. 1996) was used to further examine the minimum. A simple grid search was then used to step though the stellar mass.

For the purposes of this investigation, the input light curves were scaled in the following way: APT data were treated as Johnson B band light curves, FGS data were considered as V band, STIS data were considered R band, and MLO data were treated as I band. Using the *Hipparcos* V magnitude of 7.645 (Perryman et al. 1997) and the observed $V - I$, $R - I$, and $B - V$ color indices (Høg et al. 2000), the out-of-transit fluxes were scaled to $B = 8.18$, $V = 7.645$, $R = 7.287$, and $I = 6.985$ mag. Although the effective bandpasses of the four light curves are not equivalent to Johnson filters, these approximations are acceptable since ELC

compensates by adjusting the limb darkening parameters. Also note that the bandpasses are treated independently, i.e. the relative fluxes between them are not constrained by the blackbody temperatures, so the out-of-transit scaling can in fact be arbitrary.

4. Results and Discussion

4.1. Light Curve Fits

Figure 1 shows plots of all photometric data phase-folded and overlaid with the ELC model light curves. For this figure, the APT and MLO light curves were binned by a factor of 5 for clarity. The effect of color-dependent limb darkening is evident in the shape of the transits: the I-band light curve is considerably flatter during mid-transit than the B-band. The reduced χ^2 of each data set are the following: MLO: 1.96, STIS²: 0.95, FGS: 1.27, and APT: 1.01. The reduced χ^2_ν of the entire fit to all the observations is 1.36 with 3434 degrees of freedom. The reduced χ^2 values for the STIS and APT observations are excellent; for the MLO and FGS observations the χ^2 is high, probably as a consequence of systematic errors in the data rather than deficiencies in the model. Normalized residuals $((O - C)/\sigma)$ of the model fits are shown in Fig. 2 and, with the exception of the MLO data, show no pattern of correlated residuals. The MLO residuals do exhibit structure: just prior to mid-transit the data are generally above the model, and after mid-transit the data are below the model. We are confident this is an observational calibration problem, perhaps a residual remaining after the linear rectification.

4.2. Radial-Velocity Fit

Shown in Figure 3, the model radial velocities match the observations throughout the orbit. No obvious patterns indicative of a nonzero eccentricity are evident in the residuals. The reduced χ^2 of this model fit to the radial velocities is 2.16, though removal of one outlier at phase 0.05 lowers the χ^2_ν to 1.80. The RMS scatter of the observations about the fit is 6.6 m s^{-1} , not much larger than the mean uncertainty of 4.7 m s^{-1} in the data. We derive a stellar reflex velocity $K_{\text{star}} = 82.7 \pm 1.3 \text{ m s}^{-1}$ (note that this is independent of the assumed stellar mass). This is in good agreement with the results of Henry et al. (2000) $81.5 \pm 5.5 \text{ m s}^{-1}$.

²If we fit to the full STIS light curve, including the out-of-transit data obtained during the first HST orbit of the visit, the STIS $\chi^2_\nu = 1.54$; this is a consequence of the systematically lower flux for these unreliable data, as described in Brown et al. (2001).

s^{-1} , and marginally smaller than the values of Mazeh et al. (2000) $85.9 \pm 2.0 \text{ m s}^{-1}$ and Naef (2004) $85.1 \pm 1.0 \text{ m s}^{-1}$.

Figure 3 also shows a detailed plot of the fit to the Rossiter effect, showing the excellent agreement between the ELC model and the observations. During the transit the RMS of the residuals is 3.9 m s^{-1} , whereas the out-of-transit RMS is 8.5 m s^{-1} . The data taken during transit were all obtained on the same night (JD 2451755), whereas the remaining data come from widely separated epochs spanning more than three years. Systematics such as the long-term stability of the spectrograph are thus most likely the cause of the increased scatter outside of transit.

4.3. The Orbital Ephemeris of HD 209458b

While extremely precise, the STIS observations only span 6 nearly consecutive HD 209458b orbital cycles and therefore are not ideal for determining the ephemeris. The FGS observations span 1.3 years and hence place much tighter constraints on the period. By combining the STIS and FGS high-precision data with the ground-based observations spanning many cycles, very tight limits can be placed on the orbital period. We obtain a revised ephemeris of $T_0 = 2452854.82545 + 3.52474554E \text{ HJD}$ (Table 3). The uncertainty in period is now only 0.016 s, compared to 1.21 s (Robichon & Arenou 2000), an improvement by over a factor of 70. A comparison of our ephemeris with previously published results is shown in the O-C diagram of Fig. 4, which displays the residuals of times of mid-transit from our ephemeris. We include most previously published mid-transit times (Robichon & Arenou 2000; Charbonneau et al. 2000; Jha et al. 2000; Mazeh et al. 2000; Deeg, Garrido & Claret 2001; Schultz et al. 2003, 2004). Since we have included the STIS and FGS data in our fits, the estimates of T_0 by Schultz et al. (2004, 2003) and Brown et al. (2001) are not independent and so we cannot use the $O - C$ values in Fig. 4 to further improve the ephemeris.

Our results are in general agreement with previous work, but some discrepancies exist; for example, our period differs from (Schultz et al. 2004) by $\approx 8 \sigma$ ($\approx 0.126 \text{ sec}$). The majority of the uncertainty in the ephemeris lies in T_0 ; the uncertainty in T_0 is 750 times larger than that in the period. Clearly, if T_0 can be determined as accurately as P , attaining 1-second precision in transit timings, and hence searches for satellites and other gravitationally perturbing bodies, would be far less challenging. Despite their very high photometric precision, neither the FGS or STIS can obtain an uninterrupted observation of the 185 min transit due to HST’s low Earth orbit. This makes determining the center of transit much more difficult, and hence more uncertain. What is needed, then, are observations of *complete* transits at a precision comparable to the *Hubble Space Telescope* data, or a large set of lower-precision

mid-transit times spanning many cycles. The Canadian *MOST* satellite, expected to achieve micromagnitude photometric precision, is well-suited for this task, as its orbit enables it to continuously observe HD 209458 for many transits (Rucinski et al. 2003) with exceptionally high precision.

4.4. HD 209458 System Parameters

Given only the transit light curves and radial velocities, the absolute physical scale of the system cannot be determined and the solutions are degenerate. In Fig. 5 we show the observed relationships between the planetary and stellar radii versus the stellar mass. The solid dark curves are the ELC solutions that best match the transit and radial velocity data, and as expected, the curve follows $R \propto M_{\text{star}}^{1/3}$. Formally, a fit to the model points yields the relation $R_{\text{planet}} = 1.310 \times (M_{\text{star}})^{0.334} R_{\text{Jup}}$ and $R_{\text{star}} = 1.112 \times (M_{\text{star}})^{0.333} R_{\odot}$. The planetary and stellar radii are observationally constrained to lie along these curves, though their positions on the curve are only weakly constrained. By including Cody & Sasselov (2002)’s observationally-derived stellar radius of $1.18 \pm 0.10 R_{\odot}$ we break the degeneracy, but the uncertainty in the system scale remains large, giving a minimum uncertainty of $\pm 8\%$ in the planetary radius and 25% in the stellar mass. Our best fit value for the stellar mass using only the stellar radius constraint (along with the transit photometry, radial velocities and $V_{\text{rot}} \sin i$) is $1.25 \pm 0.35 M_{\odot}$.

If we apply the Cody & Sasselov (2002) stellar mass limit constraint, $1.06 \pm 0.13 M_{\odot}$, we limit the solutions to the light gray region in Fig. 5. The smaller, darker gray region corresponds to the mass range given by Santos et al. (2004), $1.15 \pm 0.05 M_{\odot}$. The vertical width of the gray regions correspond to the $\pm 1.6\%$ uncertainty in radius derived from the uncertainty in K_{star} . With these mass range estimates, we can robustly bracket the planetary radius to the range $1.26 - 1.42 R_{\text{Jup}}$. Note that this is not a statistical $1-\sigma$ confidence interval; solutions outside this range are highly disfavored. For comparison, we show the planetary radius estimates of Cody & Sasselov (2002), Deeg, Garrido & Claret (2001), Brown et al. (2001), and Schultz et al. (2004). The latter three studies assumed a stellar mass of $1.10 M_{\odot}$ to get the planetary radius, and so their radius ranges should be compared to the height of the gray region on our radius vs. mass curve. The box and diamond symbols show the locations of the points corresponding to the best stellar mass estimates of Cody & Sasselov (2002) and Santos et al. (2004).

The lower panel of Fig. 5 shows the family of stellar radius vs. stellar mass solutions for HD 209458. This relationship comes solely from the observations of the transit and radial velocities, and does not include any stellar astrophysics. From the transit and radial velocity

observations alone, there is no difference in goodness of fit anywhere on this curve. The mass–radius relationship for HD 209458 given by Cody & Sasselov (2002), based on stellar models, is shown as the dot–dash line (bracketed by the uncertainty in the stellar radius). As Cody & Sasselov (2002) noted, this M–R relationship is nearly orthogonal to the transit curve, and thus introduces a strong constraint on the stellar mass and radius. The intersection of the Cody & Sasselov (2002) M–R relationship with our transit–derived relationship occurs at $1.09 M_{\odot}$ and defines our “best” estimates of the stellar mass. Incorporating the uncertainty in the mass–radius relation then yields these values: $M_{\text{star}}=1.093 \pm 0.085 M_{\odot}$, $R_{\text{star}}=1.145 \pm 0.048 R_{\odot}$, and $R_{\text{planet}}=1.349 \pm 0.057 R_{\text{Jup}}$, respectively, though again we caution that the uncertainties are not statistical $1-\sigma$ confidence intervals.

We estimate a slightly higher stellar mass and smaller stellar radius than Cody & Sasselov (2002). This requires a slightly different set of adopted system parameters, e.g., we find the inclination to be 86.67 versus 86.1 degrees. But more importantly, our smaller stellar radius requires a higher temperature to produce the observed luminosity. Interestingly, Santos et al. (2004) estimate the temperature to be 6117 ± 26 K, significantly hotter than the Cody & Sasselov (2002) or Mazeh et al. (2000) value of 6000 ± 50 K. Ribas et al. (2003) also find a somewhat higher temperature, 6088 ± 56 K, as do Fischer & Valenti (2005), 6099 ± 44 K. Even a small temperature increase of 88 K requires a 3% change in radius to maintain the same bolometric luminosity, and would reduce the radius from the Cody & Sasselov (2002) value of $1.18 R_{\odot}$ to $1.145 R_{\odot}$; a 117 K increase in effective temperature would drop the radius to $1.136 R_{\odot}$; both of these agree well with our stellar radius estimate, suggesting stellar temperatures greater than 6000 K are favored. These higher temperatures imply a slightly earlier spectral type, F9, than the usual adopted value of G0 (see e.g. Gray, Napier & Winkler (2001) and Gray, Graham & Hoyt (2001)).

A higher temperature would also mean a younger age, as can be seen in the stellar evolution tracks shown in Fig. 1 of Cody & Sasselov (2002): the observation box would be shifted to the left, and closer to the main sequence. However, the slightly younger age makes little difference to the planetary radius predicted from planetary evolution, since the shrinking of the planet vs. time is quite slow after a few billion years.

As a check, we estimated the stellar radius from the *Hipparcos* parallax–derived distance, the observed magnitudes (assuming zero reddening), the observed surface gravity (Santos et al. 2004), an assumed effective temperature, and synthetic photometry computed from the NEXTGEN stellar models (Hauschildt et al. 1999). These stellar radius estimates are shown in Fig. 5, for $T_{\text{eff}}=6000$ K and 6117 K. Also shown are the stellar radius estimates of Cody & Sasselov (2002), Allende Prieto & Lambert (1999), and Ribas et al. (2003); all are consistent within their uncertainties and with our “best” mass and radius estimate. In particular, the

optical–IR synthetic photometry technique employed by Ribas et al. (2003) gives a stellar radius of $1.145 \pm 0.049 R_{\odot}$ in excellent agreement with our favored estimate.

It is interesting that the Cody & Sasselov (2002) planet radius estimate is notably larger than our value, despite our heavy reliance on their stellar radius estimate to set the physical scale of the system. Using our transit–derived radius vs. mass relation, their stellar radius estimate ($1.18 R_{\odot}$) is inconsistent with their preferred stellar mass ($1.06 M_{\odot}$); a larger stellar mass, $1.20 M_{\odot}$, is required for consistency with our transit modelling. For completeness, we note that the radius vs. mass relationship derived by Deeg, Garrido & Claret (2001), $R_{\text{star}} = 0.34M_{\text{star}} + 0.825 (\pm 0.06)$, gives a stellar radius larger by $\sim 0.05 R_{\odot}$ than our results, and hence their system scale is larger by approximately this amount. Their estimate was made prior to the exquisite *Hubble Space Telescope* transit observations and the tighter constraints those observations provide; our stellar radius vs. mass relation is similar to their lower $1-\sigma$ limit on the relation.

Just as with the planetary radius, the planetary mass depends on the adopted stellar mass. The transit and radial velocity data constrain the planetary mass to lie along a curve; formally we find $M_{\text{planet}} = 0.620 \times (M_{\text{star}})^{0.670} M_{\text{Jup}}$ from our model fits. This is exactly what is expected for circular Keplerian orbits and mass ratio $Q \gg 1$: $M_{\text{planet}} = (P/2\pi G)^{1/3} (K_{\text{star}} / \sin i) \times (M_{\text{star}})^{2/3}$. Applying the stellar mass–radius constraint as above, we find $M_{\text{planet}} = 0.658 \pm 0.034 M_{\text{Jup}}$.

In Table 4, we present the system parameters as a function of stellar mass for three representative cases, $M_{\text{star}} = 0.93$, 1.07 , and $1.19 M_{\odot}$. These cases bracket the full range in stellar mass that is deemed acceptable, following Cody & Sasselov (2002). The overall reduced χ^2 of the fit to the 3434 observations (transit photometry, radial velocities, R_{star} , and $V_{\text{rot}} \sin i$) was 1.364. Because of the degeneracy of the solutions discussed above, the χ^2 does not vary significantly across this mass range.

Our system parameter values are generally in good agreement with those derived in previous work. Our estimate of the planetary radius is strongly constrained to be between $1.26 - 1.42 R_{\text{Jup}}$, using the stellar mass limits of Cody & Sasselov (2002) and Santos et al. (2004). Applying the stellar mass–radius relation of Cody & Sasselov (2002), we get much tighter limits: $1.35 \pm 0.06 R_{\text{Jup}}$. This radius is consistent with previously published results (Brown et al. 2001; Cody & Sasselov 2002; Schultz et al. 2004; Deeg, Garrido & Claret 2001; Laughlin et al. 2005), and hence the discrepancy between the observed and theoretical models of extrasolar giant planets remains. The planetary radius is 20% larger than evolutionary models which only include irradiation (e.g. Burrows et al. (2003), Chabrier et al. (2004)); these give a radius of $\sim 1.1 R_{\text{Jup}}$, equal to the bottom edge of the top panel in Fig. 5, and firmly ruled out. As suggested by Bodenheimer, Lin, & Mardling (2001),

eccentricity pumping, perhaps by an additional planet, may provide the energy needed to inflate the radius of HD 209458b. However, the radial-velocity residuals currently do not support a significant nonzero eccentricity. The recent observation of the secondary eclipse of HD 209458b by Deming et al. (2005) also strongly supports an eccentricity indistinguishable from zero, as the timing of the secondary eclipse is not significantly displaced from phase 0.5. Thus the observed radius of HD 209458b remains unsatisfactorily explained and continues to demonstrate deficiencies in our understanding of irradiated extrasolar giant planet evolution. Finally, with a mass of $0.66 \pm 0.03 M_{\text{Jup}}$ and the above radius, the mean density of HD 209458b is $0.33 \pm 0.05 \text{ g cm}^{-3}$, about half the density of Saturn and one-fourth the density of Jupiter; HD 209458b is a very low density gas giant planet.

5. Summary

We have used the ELC code Orosz & Hauschildt (2000) to determine the system parameters of HD 209458 by simultaneously fitting the transit light curves and radial velocities. The observations consist of the *Hubble Space Telescope* STIS (Brown et al. (2001)) and FGS (Schultz et al. (2004)) light curves, plus 18 transits obtained over 4 years with the facilities at MLO and APT, along with Keck HIRES spectroscopic radial velocities. Our new estimates of the system parameters are generally in agreement with previous results, e.g., $1.26 < R_{\text{planet}} < 1.42 R_{\text{Jup}}$ and $0.59 < M_{\text{planet}} < 0.70 M_{\text{Jup}}$. We stress that this range includes the uncertainty in the stellar mass. By applying the mass-radius relation of Cody & Sasselov (2002), we reduce the uncertainty substantially: $R_{\text{planet}} = 1.35 \pm 0.06 R_{\text{Jup}}$, $M_{\text{planet}} = 0.66 \pm 0.03 M_{\text{Jup}}$. Our results confirm that the planetary radius remains significantly larger (20%) than predicted by irradiated planet evolution models (e.g. Burrows et al. (2003)). For the stellar parameters, we find $M_{\text{star}} = 1.09 \pm 0.09 M_{\odot}$ and $R_{\text{star}} = 1.15 \pm 0.05 R_{\odot}$.

We have also obtained an orbital ephemeris with a period determination good to 0.016 s, over 70 times more precise than the period by Robichon & Arenou (2000). An ephemeris of this precision should facilitate future searches for additional bodies in the HD 209458 system. In addition to increasing the precision of HD 209458 system parameters, we believe we have made improvements to the accuracy as well. By using ELC, a fully self-consistent dynamical model that includes subtle physical effects not contained in previous work, we have reduced systematic errors. As observational precision increases, and detection methods become sensitive to smaller planets at larger orbital distances (ultimately to Earth analogs), the need for such exactitude in the modelling is warranted.

The authors wish to thank Drs. E. L. Robinson, K. Horne and P. Hauschildt for useful

discussions related to this work. We also thank Ms. D. Martino and S. Airieau for assistance in obtaining transit observations at MLO. GWH acknowledges support from NASA grant NCC5-511 and NSF grant HRD 97-06268, and WFW acknowledges support by an award from Research Corporation. This research has made use of NASA’s Astrophysics Data System (ADS), the SIMBAD database, operated at CDS, Strasbourg, France, NASA’s SkyView (<http://skyview.gsfc.nasa.gov>) and Dr. John Thorstensen’s SkyCalc software. Observations obtained at MLO made use of the HPWREN (“High Performance Wireless Research and Education Network”) sponsored by the NSF ANIR division under grant ANI-0087344 and the University of California San Diego. We are greatly indebted to D. Charbonneau et al. for providing the *Hubble Space Telescope* STIS photometry.

REFERENCES

Agol, E., Steffen, J., Sari, R., & Clarkson, W. 2005, MNRAS, 295, ??? (astro-ph/0412032)

Allende Prieto, C., & Lambert, D. L. 1999, A&A, 352, 555

Alonso, R., et al. 2004, ApJ, 613, L153

Baraffe, I., Chabrier, G., Barman, T. S., Allard, F., & Hauschildt, P. H. 2003, A&A, 402, 701

Bodenheimer, P., Lin, D. N. C., & Mardling, R. A. 2001, ApJ, 548, 466

Bodenheimer, P., Laughlin, G., & Lin, D. N. C. 2003, ApJ, 592, 555

Brown, T. M., Charbonneau, D., Gilliland, R. L., Noyes, R. W., & Burrows, A. 2001, ApJ, 552, 699

Bundy, K. A. & Marcy, G. W. 2000, PASP, 112, 1421

Burrows, A., Hubeny, I., Hubbard, W. B., Sudarsky, D., & Fortney, J. J. 2004, ApJ, 610, L53

Burrows, A., Sudarsky, D., Hubbard, W. B. 2003, ApJ, 594, 545

Butler, R. P., Marcy, G. W., Williams, E., McCarthy, C., Dosanjh, P., & Vogt, S. S. 1996, PASP, 108, 500

Chabrier, G., Barman, T., Baraffe, I., Allard, F., & Hauschildt, P. H. 2004, ApJ, 603, L53

Charbonneau, D., Brown, T. M., Latham, D. W., & Mayor, M. 2000, ApJ, 529, L45

Charbonneau, P. 1995, *ApJS*, 101, 309

Cho, J. Y.-K., Menou, K., Hansen, B. M. S., & Seager, S. 2003, *ApJ*, 587, L117

Claret, A. 2000, *A&A*, 363, 1081

Cody, A. M., & Sasselov, D. D. 2002, *ApJ*, 569, 451

Deeg, H. J., Garrido, R., & Claret, A. 2001, *New Astronomy*, 6, 51

Deming, D., Seager, S., Richardson, L. J., & Harrington, J. 2005, *Nature*, 434, 740

Eaton, J. A., Henry, G. W., & Fekel, F. C. 2003, in *The Future of Small Telescopes in the New Millennium II. The Telescopes We Use*, ed. T. Oswalt (Dordrecht: Kluwer), 189

Fischer, D. A., & Valenti, J. 2005, *ApJ*, 622, 1102

Gray, R. O., Napier, M. G., & Winkler, L. I. 2001, *AJ*, 121, 2148

Gray, R. O., Graham, P. W., & Hoyt, S. R. 2001, *AJ*, 121, 2159

Guillot, T., & Showman, A. P. 2002, *A&A*, 385, 156

Hauschildt, P. H., Allard, F., & Baron, E. 1999, *ApJ*, 512, 377

Henry, G. W. 1999, *PASP*, 111, 845

Henry, G. W., Marcy, G. W., Butler, R. P., & Vogt, S. S. 2000, *ApJ*, 529, L41

Høg, E., et al. 2000, *A&A*, 355, L27

Holman, M.J. & Murray, N.W. 2004, *astro-ph/0412028*

Jha, S., Charbonneau, D., Garnavich, P. M., Sullivan, D. J., Sullivan, T., Brown, T. M., & Tonry, J. L. 2000, *ApJ*, 540, L45

Laughlin, G., Wolf, A., Vanmunster, T., Bodenheimer, P., Fischer, D., Marcy, G., Butler, R., & Vogt, S. 2005, *ApJ*, 621, 1072

Marcy, G. W. & Butler, R. P. 1992, *PASP*, 104, 270

Mazeh, T. et al. 2000, *ApJ*, 532, L55

Menou, K., Cho, J. Y.-K., Seager, S., & Hansen, B. M. S. 2003, *ApJ*, 587, L113

Naef, D., Mayor, M., Beuzit, J. L., Perrier, C., Queloz, D., Sivan, J. P., & Udry, S. 2004, A&A, 414, 351

Orosz, J. A., & Hauschildt, P. H. 2000, A&A, 364, 265

Orosz, J. A., Groot, P. J., van der Klis, M., McClintock, J. E., Garcia, M. R., Zhao, P., Jain, R. K., Bailyn, C. D., & Remillard, R. A. 2002, ApJ, 568, 845

Perryman, M. A. C., et al. 1997, A&A, 323, L49

Press, W. H., Teukolsky, S. A., Vetterling, W. T. & Flannery, B. P. 1996, Numerical Recipes in Fortan 77, Vol 1 (2nd ed.; New York: Cambridge Univ. Press)

Queloz, D., Eggenberger, A., Mayor, M., Perrier, C., Beuzit, J. L., Naef, D., Sivan, J. P., & Udry, S. 2000, A&A, 359, L13

Ribas, I., Solano, E., Masana, E., & Gimnez, A. 2003, A&A, 411, L501

Robichon, N., & Arenou, F. 2000, A&A, 355, 295

Rossiter, R. A. 1924, ApJ, 60, 15

Rucinski, S., Carroll, K., Kuschnig, R., Matthews, J., & Stibrany, P. 2003, Advances in Space Research, 31, 371

Sanotos, N. C., Israelian, G., & Mayor, M. 2004, A&A, 415, 1153

Sartoretti, P., & Schneider, J. 1999, A&AS, 134, 553

Schultz, A.B. et al. 2004, in *The Search For Other Worlds*, AIP Conf. Proc. 713, 161

Schultz, A. et al. 2003, in *Scientific Frontiers in Research on Extrasolar Planets*, ASP Conference Series v. 294, eds. D. Deming and S. Seager, p. 479.

Showman, A. P. & Guillot, T. 2002, A&A, 385, 166

Sozzetti, A., et al. 2004, ApJ, 616, L167

Valenti, J. A., Butler, R. P., & Marcy, G. W. 1995, PASP, 107, 966

van Hamme, W. 1993, AJ, 106, 2096

von Zeipel, H. 1924, MNRAS, 84, 702

Williams, D.M., Kasting, J.F., Wade, R.A. 1997, Nature, 385, 234.

Wilson, R. E., & Sofia, S. 1976, ApJ, 203, 182

Table 1. Observation Log

Instrument	UT Date	Start Time (HJD-2450000)
MLO	2001 Jun 29-30	2089.840
MLO	2001 Oct 13	2195.636
MLO	2002 Jun 13	2438.836
MLO	2002 Aug 5	2491.736
MLO	2002 Aug 12	2498.726
MLO	2002 Sep 27	2544.626
MLO	2002 Oct 4	2551.640
MLO	2002 Oct 11	2558.616
MLO	2002 Oct 18	2565.681
MLO	2002 Dec 10	2618.585
MLO	2003 Jul 27	2847.776
MLO	2003 Aug 3	2854.718
STIS	2000 Apr 25	1659.744
STIS	2000 Apr 28-29	1663.297
STIS	2000 May 5-6	1670.336
STIS	2000 May 12-13	1677.376
FGS	2001 Jun 11	2072.274
FGS	2001 Sep 11-12	2163.902
FGS	2001 Nov 10	2223.793
FGS	2002 Jan 16	2290.783
FGS	2002 Sep 30	2548.085
T8 APT	2001 Oct 6	2188.592
T8 APT	2001 Oct 13	2195.579
T10 APT	2002 Oct 4	2551.589
T10 APT	2002 Oct 11	2558.581
T10 APT	2004 Sep 15	3263.606
T10 APT	2004 Sep 22	3270.597

Table 2. ELC Model Input Constraints

Parameter	Value	Reference or Reason
T_{eff} , star	6000 K	Cody & Sasselov (2002)
T_{eff} , planet	1300 K	Guillot & Showman (2002)
Orbital eccentricity e	0.00	Mazeh et al. (2000)
Planet rotation/orbital frequency (Ω_{planet})	1.00	Assume tidal locking
Radius of star R_{star}	$1.18 \pm 0.10 \text{ R}_{\odot}$	Cody & Sasselov (2002)
Rotational velocity of star $V_{\text{rot}} \sin i$	$3.75 \pm 1.25 \text{ km s}^{-1}$	Queloz et al. (2000)

Table 3. HD 209458b Ephemeris

Parameter	Value & Uncertainty
T_0 (HJD)	$2452854.82545 \pm 1.35 \times 10^{-4}$
Period (days)	$3.52474554 \pm 1.8 \times 10^{-7}$

Table 4. HD 209458 System Parameters

Parameter	Estimate		
M_{star} (M_{\odot})	0.93	1.07	1.19
R_{star} (R_{\odot})	1.085	1.137	1.178
M_{planet} (M_{Jup})	0.590	0.649	0.697
R_{planet} (R_{Jup})	1.279	1.340	1.388
Inclination (degrees)	86.668	86.668	86.668
K_{star} (m/s)	82.6	82.7	82.7
Orbital separation (AU)	0.044	0.046	0.048
Limb-darkening coefficients			
$x(B)$	0.869	0.859	0.868
$y(B)$	0.269	0.248	0.267
$x(V)$	0.724	0.725	0.724
$y(V)$	0.328	0.329	0.328
$x(R)$	0.774	0.776	0.775
$y(R)$	0.434	0.436	0.436
$x(I)$	0.814	0.809	0.814
$y(I)$	0.628	0.616	0.627
χ^2 (3434 degrees of freedom)	4682.4	4682.3	4681.4
χ^2_{ν}	1.364	1.364	1.363

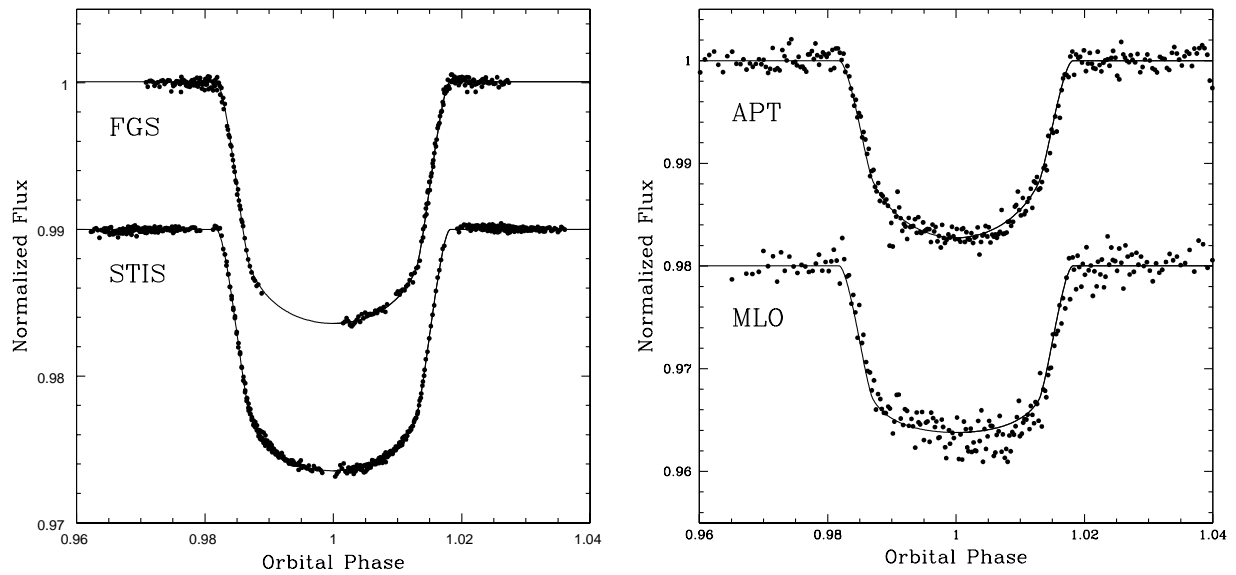


Fig. 1.— Light curves and model fit, in normalized flux units (with arbitrary offset) folded on our ephemeris. The orbital phases shown here span 6.7 hours and each tick mark corresponds to 25 minutes. Left panel: HST FGS and STIS observations. Right panel: Ground-based APT and MLO observations.

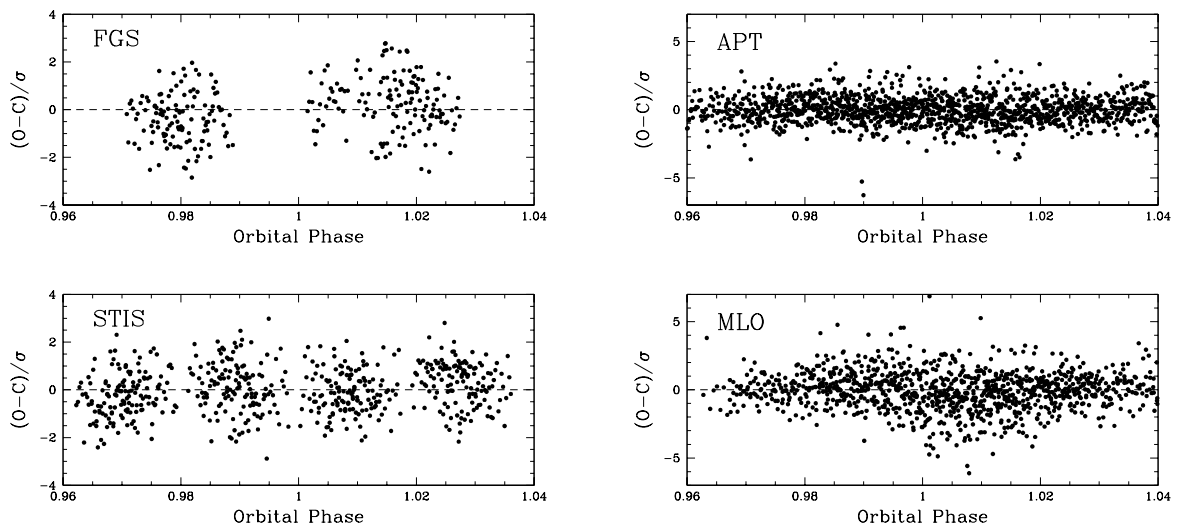


Fig. 2.— Left panel: Normalized residuals ($\chi \equiv (O - C)/\sigma$) of ELC model fit to FGS and STIS data sets. Right panel: Normalized residuals for APT and MLO data sets.

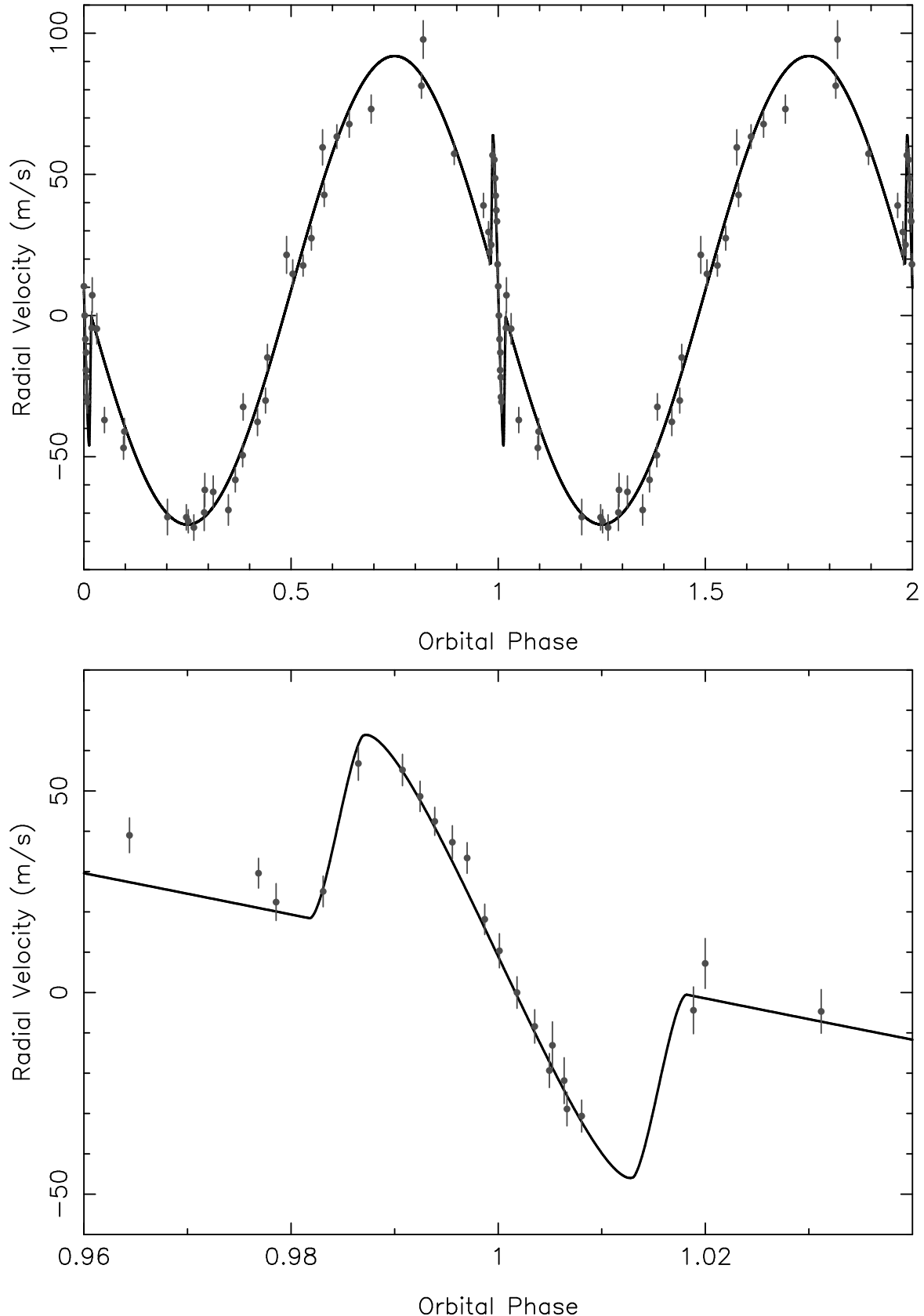


Fig. 3.— Top panel: Radial velocity curve and model fit. Bottom panel: Expanded view of the Rossiter effect during transit.

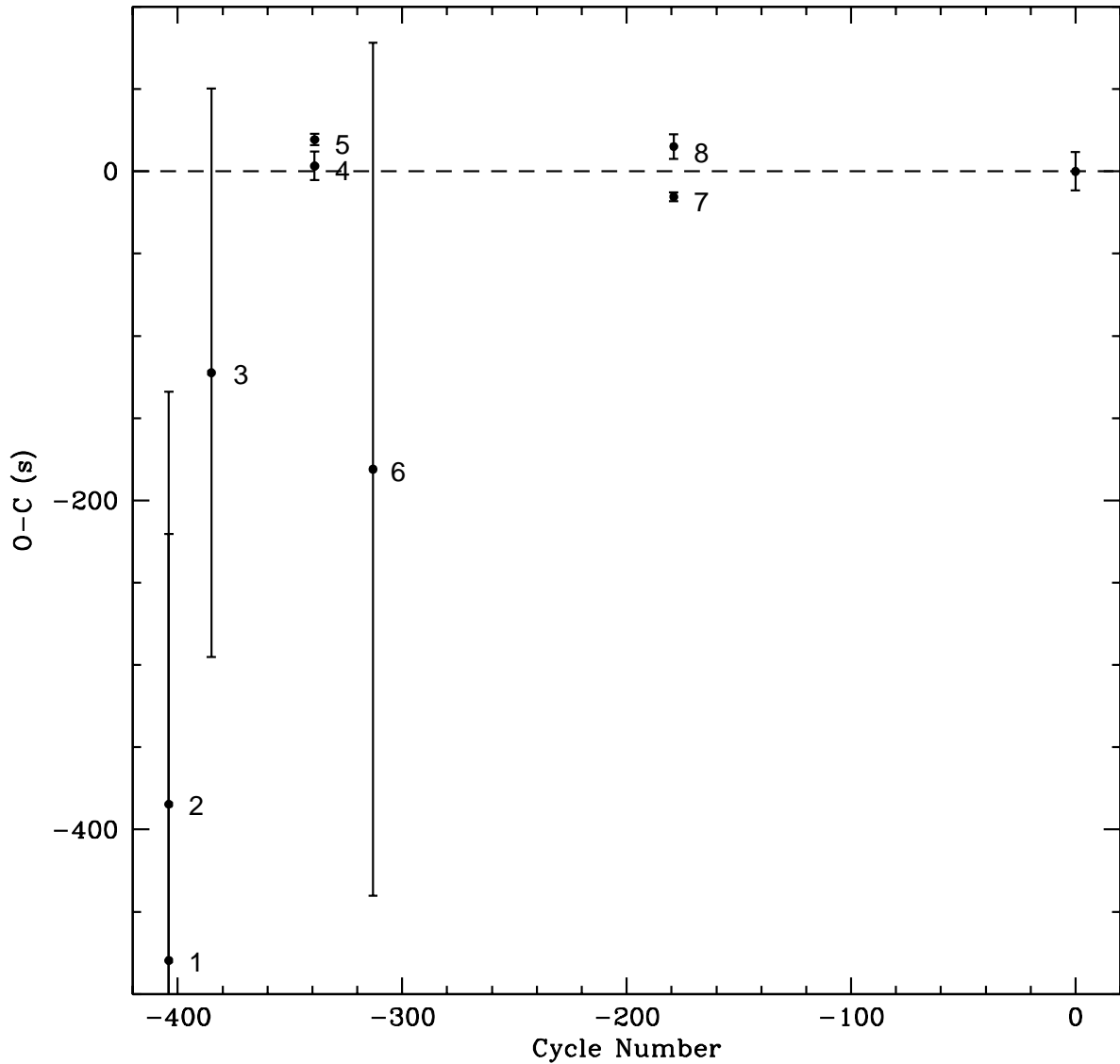


Fig. 4.— O-C diagram of published transit times. 1: Charbonneau et al. (2000), 2: Mazeh et al. (2000), 3: Jha et al. (2000), 4: STIS (Schultz et al. 2003), 5: STIS (Brown et al. 2001), 6: estimated from Deeg, Garrido & Claret (2001) Figure 1, 7: FGS & STIS (Schultz et al. 2004), 8: FGS (Schultz et al. 2003). Our result is shown at cycle 0.

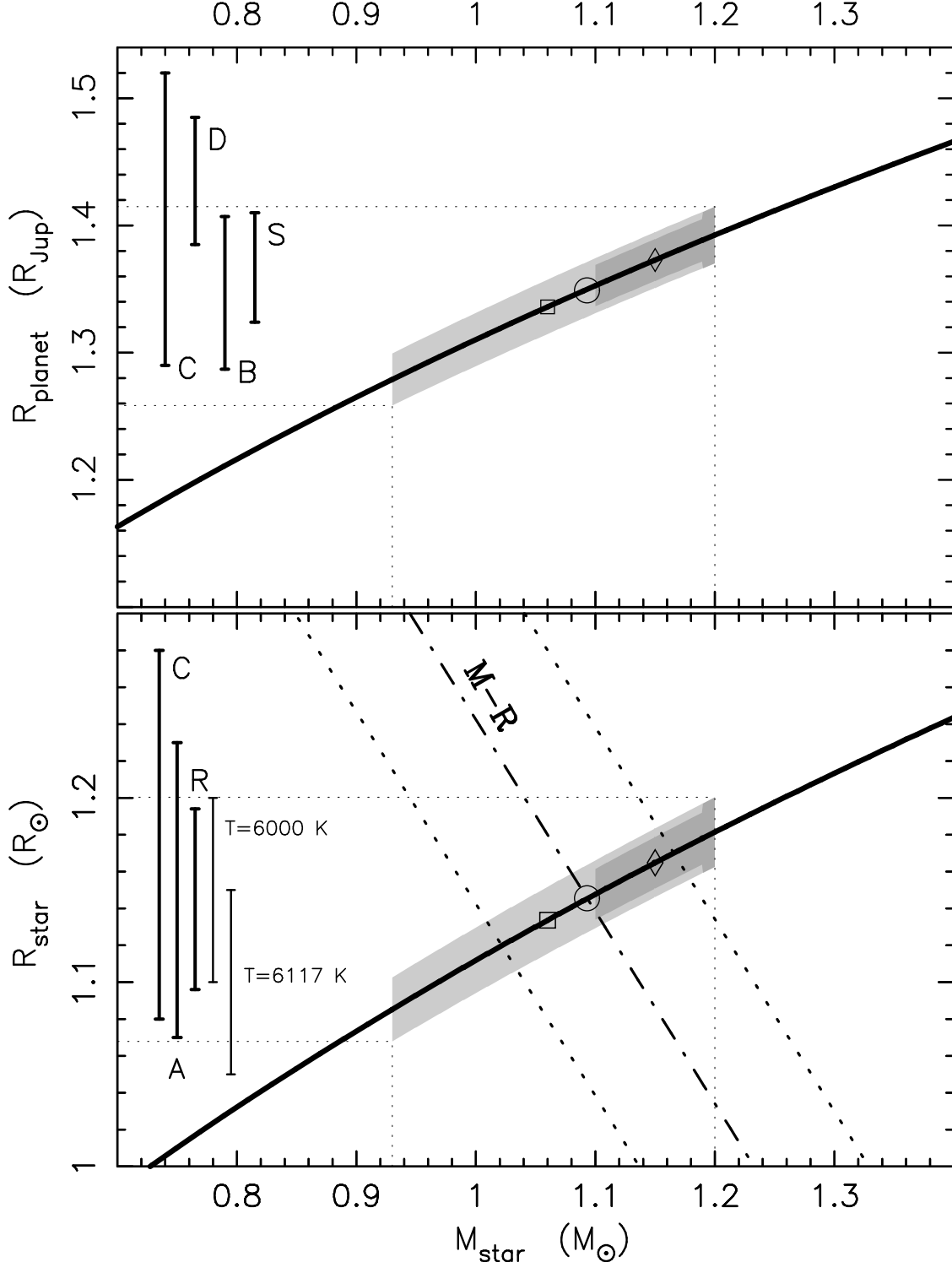


Fig. 5.— Planetary and stellar radii versus stellar mass, as determined by the transit and radial velocity data. The shaded regions show acceptable solutions when a stellar mass constraint is used (light gray = Cody & Sasselov (2002), dark gray = Santos et al. (2004)). For comparison, several published radius estimates are shown. The dot-dash line in the lower panel is the mass-radius relationship of Cody & Sasselov (2002). Being nearly orthogonal to the transit-derived relationship, this strongly constrains the solutions.

Table 5. Appendix A. HD 209458 Radial Velocities

JD-2440000	Velocity (m/s)	Uncertainty (m/s)
11341.120	27.4082	4.27456
11368.941	-14.8687	4.70025
11372.134	-68.8846	5.43136
11373.056	63.3803	4.23387
11374.055	57.3234	3.83308
11410.012	-46.8673	4.08451
11410.963	-58.2164	4.31140
11411.933	67.8324	4.70083
11438.808	-75.1139	4.50866
11543.689	-4.40406	5.81311
11543.693	7.22008	6.19649
11550.691	-13.0944	5.84085
11550.695	-21.8537	5.68874
11551.696	-69.7612	6.43132
11551.701	-61.8012	5.90380
11552.703	59.5577	6.27228
11679.107	-30.1170	4.43266
11703.121	-72.8776	4.12058
11704.098	17.7321	3.79917
11705.105	81.4237	4.44392
11706.102	-41.1026	4.67668
11707.108	-49.4668	4.12699
11754.975	38.9955	4.31567
11755.019	29.5864	3.70445
11755.025	22.4362	4.57242
11755.041	25.0708	3.80745
11755.053	56.8067	4.17220
11755.068	55.1958	3.89396
11755.074	48.6594	3.76043
11755.079	42.4521	3.48089
11755.085	37.2782	4.10421
11755.090	33.3655	3.80314
11755.096	18.1643	3.77334
11755.101	10.3582	4.24120
11755.107	0.00000	3.91536
11755.113	-8.40466	4.15610
11755.118	-19.3426	4.23024
11755.124	-28.8793	4.18412
11755.129	-30.6304	3.96976
11755.972	-71.4988	4.49593
11792.791	73.1506	4.99995
11882.707	-71.3874	6.32029
11883.720	21.4772	6.54957
11899.731	-4.68023	5.41906
11900.721	-62.4702	5.65784

Table 5—Continued

JD-2440000	Velocity (m/s)	Uncertainty (m/s)
12063.112	-32.3614	4.72176
12102.004	-37.6616	4.88177
12446.128	-37.0244	4.48457
12514.965	42.7284	4.14144
12535.845	14.7720	4.96706
12575.730	97.7788	6.70706